Acta Materialia 156 (2018) 196–204

Contents lists available at ScienceDirect

Acta Materialia

journal homepage: www.elsevier.com/locate/actamat

Full length article

Measurement of anisotropic coefficients of thermal expansion of SAC305 solder using surface strains of single grain with arbitrary orientation

Bulong Wu [a], Yu-Hsiang Yang [a], Bongtae Han [a, *], Joshua Schumacher [b]

[a] Mechanical Engineering Department, University of Maryland College Park, MD, 20742, United States
[b] Center for Nanoscale Science and Technology, National Institute of Standards and Technology, Gaithersburg, MD, 20899, United States

ARTICLE INFO

Article history:
Received 6 June 2018
Accepted 14 June 2018
Available online 20 June 2018

Keywords:
SAC305
Coefficient of thermal expansion
Grain orientation
Moiré interferometry

ABSTRACT

The anisotropic coefficient of thermal expansions (CTEs) of SAC305 grain are measured using a full-field in-plane displacement measurement technique. Theoretical relationships among (1) the transversely-isotropic CTEs, (2) the surface strains of a specimen containing a single grain with arbitrary orientation, and (3) the direction of a grain orientation are derived first. Cube shape specimens that contain a single SAC305 grain are fabricated by controlling cooling rates. Thermally-induced displacements fields with a sub-micron resolution are documented on two perpendicular surfaces of the specimen as a function of temperature, and the engineering strains are calculated from the displacement fields. Two directional CTE values are determined from the theoretical relationships. The direction of the *c*-axis is also obtained during CTE calculations. The validity of the measurement is corroborated by comparing the *c*-axis direction obtained from the experiment with a grain orientation measured by the electron backscatter diffraction (EBSD) method.

1. Introduction

Since Pb was banned for the majority of manufactured electronics, hypoeutectic Pb-free solder, such as Sn3.0Ag0.5Cu (SAC305) and Sn1.0Ag0.5Cu (SAC105) solder alloys, have been widely accepted because they are cost-effective and offer performance like ternary near-eutectic SAC387 solder alloy [1]. The hypoeutectic SAC305 solder alloy contains 96.5% of Sn, and intermetallic compounds (IMCs) of Ag_3Sn and Cu_6Sn_5 disperse around β-Sn grain matrix.

The mechanical behavior of SAC305 is quite different from the traditional eutectic Sn63Pb37 solder. The Sn63Pb37 solder contains soft islands of Pb embedded in Sn matrix [1], and it has been treated as a homogenous material with isotropic properties for stress analyses since its grain size is relatively small [2,3]. However, Sn grains in SAC solders are large, and some solder joints of surface-mount components contain only two or three grains [1,4–10].

Sn crystal has a body-central tetragonal (BCT) structure (Fig. 1) with the lattice constants of $a = b = 1.833c$. Anisotropic elastic modulus and the coefficient of thermal expansion (CTE) of Sn unit cell can vary by a factor of 3 and 2, respectively [6,7].

It has been reported that β-Sn has transversely isotropic CTE values [11,12]. The CTE value on the plane perpendicular to the *c*-axis (Fig. 1) of a Sn grain is isotropic; i.e., the CTE is the same along any direction on the (001) plane (will be referred to as α_a). The CTE value along the *c*-axis ([001] direction), α_c, is different from α_a. As a result, SAC305 solder joints are expected to have strong anisotropic thermal expansion responses since they contain a large amount of Sn [6,7,9,10,13]. To the best knowledge of the authors, however, the anisotropic CTE values of SAC305 solder grains have not been measured experimentally.

In this work, the anisotropic CTEs of SAC305 grains are measured uniquely using a full-field in-plane displacement measurement technique called moiré interferometry. Cube shape specimens that contain a single SAC305 grain are fabricated by controlling cooling rates. Thermally-induced displacements fields with a sub-micron resolution are documented on two perpendicular surfaces of the specimen as a function of temperature, and the engineering strains are calculated from the displacement fields. Then, directional CTE values are determined from theoretical relationships among (1) the transversely-isotropic CTEs, (2) the

* Corresponding author.
E-mail address: bthan@umd.edu (B. Han).

https://doi.org/10.1016/j.actamat.2018.06.032
1359-6454/

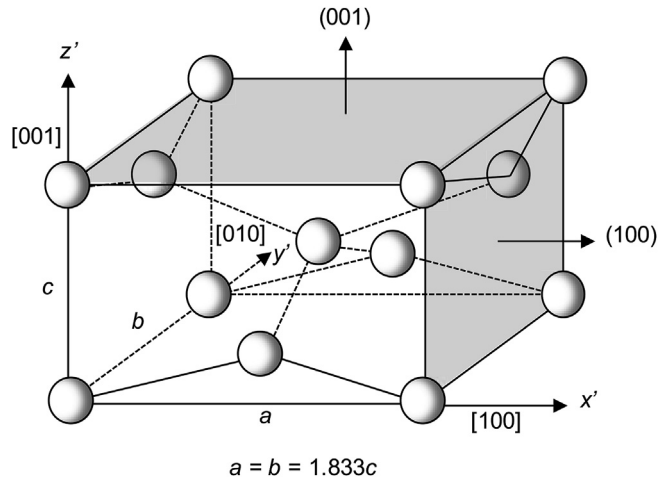

Fig. 1. Illustration of β-Sn crystal structure.

surface strains of a specimen containing a single grain with arbitrary orientation, and (3) the direction of a grain orientation.

The theoretical relationships are described first before briefly reviewing moiré interferometry. The test results are followed with the detailed description of specimen preparation. The validity of the measurement is corroborated by the grain orientation obtained by the electron backscatter diffraction (EBSD) method.

2. Theoretical relationships

Theoretical relationships are described first. Then, a procedure to determine the directional CTE values and the direction of a grain orientation from the surface strains measured on two perpendicular surfaces is presented.

2.1. Governing relationships

Fig. 2 shows the specimen coordinate (o-xyz) and the coordinate of a grain with arbitrary orientation (o-$x'y'z'$). The blue and red blocks represent the specimen and the solder grain orientation, respectively.

In the grain coordinate, the c-axis is aligned with the z' axis, and the a-axis and b-axis are aligned with the x', y' axis, respectively. The specimen coordinate can be transformed into the solder grain coordinate through three sequential steps of coordinate rotation, schematically illustrated in Fig. 3: step 1: the xyz coordinate rotates around the z-axis by angle A_1, and transforms into the $x_1y_1z_1$ coordinate; step 2: the $x_1y_1z_1$ coordinate rotates around the x_1-axis by angle A_2, and transforms into the $x_2y_2z_2$ coordinate; and step 3: the $x_2y_2z_2$ coordinate rotates around the z_2-axis by angle A_3, and transforms into the grain coordinate, the $x'y'z'$ coordinate, where A_1, A_2 and A_3 are Euler angles.

The transformation matrix can be determined as:

$$\tilde{T} = R_{A3}R_{A2}R_{A1} = \begin{bmatrix} \cos A_3 \cos A_1 - \sin A_3 \cos A_2 \sin A_1 & \cos A_3 \sin A_1 + \sin A_3 \cos A_2 \cos A_1 & \sin A_3 \sin A_2 \\ -\sin A_3 \cos A_1 - \cos A_3 \cos A_2 \sin A_1 & -\sin A_3 \sin A_1 + \cos A_3 \cos A_2 \cos A_1 & \cos A_3 \sin A_2 \\ \sin A_2 \sin A_1 & -\sin A_2 \cos A_1 & \cos A_2 \end{bmatrix} \quad (1)$$

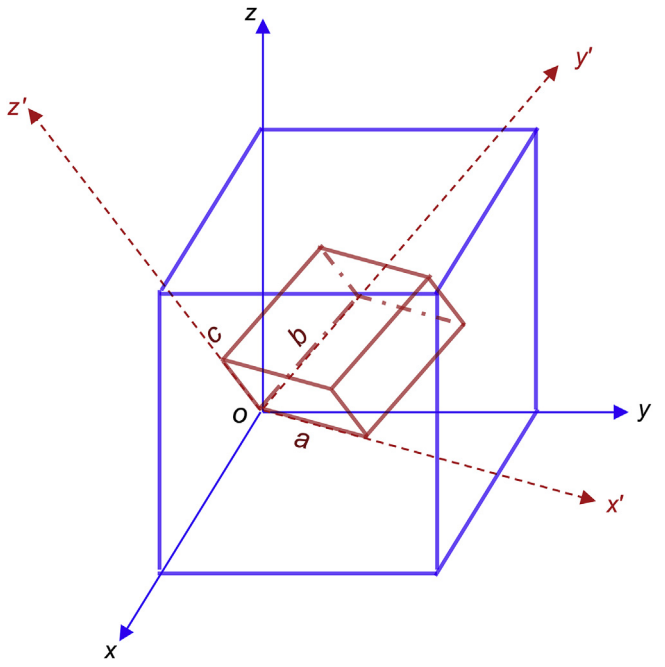

Fig. 2. Solder specimen coordinate (o-xyz) and grain coordinate (o-$x'y'z'$).

where

$$R_{A1} = \begin{bmatrix} \cos A_1 & \sin A_1 & 0 \\ -\sin A_1 & \cos A_1 & 0 \\ 0 & 0 & 1 \end{bmatrix},$$

$$R_{A2} = \begin{bmatrix} 1 & 0 & 0 \\ 0 & \cos A_2 & \sin A_2 \\ 0 & -\sin A_2 & \cos A_2 \end{bmatrix}, R_{A3} = \begin{bmatrix} \cos A_3 & \sin A_3 & 0 \\ -\sin A_3 & \cos A_3 & 0 \\ 0 & 0 & 1 \end{bmatrix}.$$

The thermal strain tensor at the grain coordinate can be expressed as:

$$\tilde{\varepsilon}' = \begin{bmatrix} \varepsilon_{x'x'} & \varepsilon_{x'y'} & \varepsilon_{x'z'} \\ \varepsilon_{y'x'} & \varepsilon_{y'y'} & \varepsilon_{y'z'} \\ \varepsilon_{z'x'} & \varepsilon_{z'y'} & \varepsilon_{z'z'} \end{bmatrix} = \begin{bmatrix} \alpha_a \cdot \Delta T & 0 & 0 \\ 0 & \alpha_a \cdot \Delta T & 0 \\ 0 & 0 & \alpha_c \cdot \Delta T \end{bmatrix} \quad (2)$$

where ΔT is the temperature change; α_c and α_a are the CTE values along the c-axis and a-axis, respectively.

The strain tensor at the specimen coordinate can be determined by:

$$\tilde{\varepsilon} = \begin{bmatrix} \varepsilon_{xx} & \varepsilon_{xy} & \varepsilon_{xz} \\ \varepsilon_{yx} & \varepsilon_{yy} & \varepsilon_{yz} \\ \varepsilon_{zx} & \varepsilon_{zy} & \varepsilon_{zz} \end{bmatrix} = \tilde{T}^T \tilde{\varepsilon}' \tilde{T} \quad (3)$$

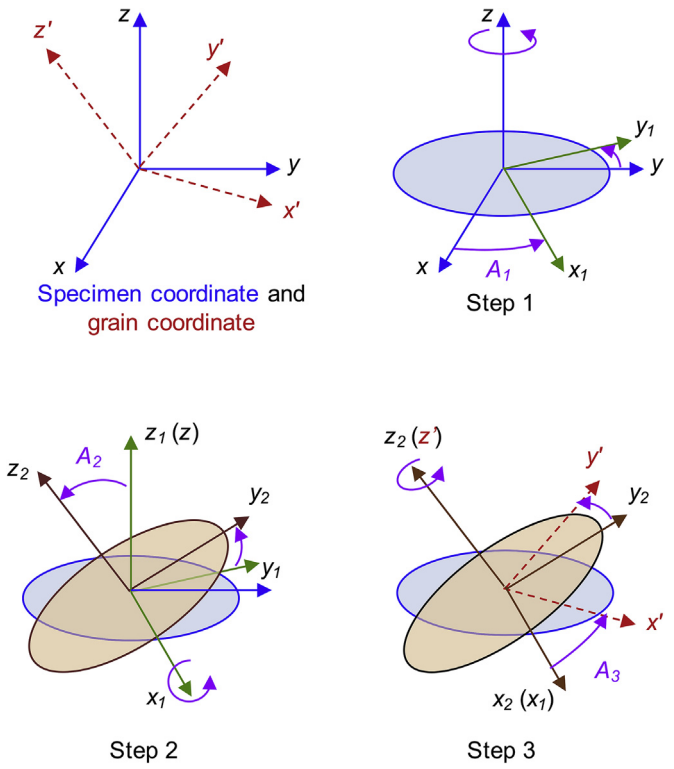

Fig. 3. Illustration of three sequential steps of coordinate transformation.

From Eqs. (1)–(3), the engineering strains of specimen surfaces can be expressed in terms of $\varepsilon_{x'x'}$, $\varepsilon_{z'z'}$, A_1 and A_2 as:

$$\begin{cases} \varepsilon_x = \varepsilon_{xx} = \left(\cos^2 A_2 \cdot \sin^2 A_1 + \cos^2 A_1\right)\varepsilon_{x'x'} + \sin^2 A_1 \cdot \sin^2 A_2 \varepsilon_{z'z'} \\ \varepsilon_y = \varepsilon_{yy} = \left(\cos^2 A_2 \cdot \cos^2 A_1 + \sin^2 A_1\right)\varepsilon_{x'x'} + \cos^2 A_1 \cdot \sin^2 A_2 \varepsilon_{z'z'} \\ \varepsilon_z = \varepsilon_{zz} = \left(\sin^2 A_2\right)\varepsilon_{x'x'} + \cos^2 A_2 \varepsilon_{z'z'} \\ \gamma_{xy} = 2\varepsilon_{xy} = 2\sin^2 A_2 \cdot \sin A_1 \cdot \cos A_1 (\varepsilon_{x'x'} - \varepsilon_{z'z'}) \\ \gamma_{xz} = 2\varepsilon_{xz} = 2\sin A_2 \cdot \cos A_2 \cdot \sin A_1 (\varepsilon_{z'z'} - \varepsilon_{x'x'}) \\ \gamma_{yz} = 2\varepsilon_{yz} = 2\sin A_2 \cdot \cos A_2 \cdot \cos A_1 (\varepsilon_{x'x'} - \varepsilon_{z'z'}) \end{cases} \tag{4}$$

2.2. Determination of anisotropic CTE values from surface strains

The principal strains and the principal angle of the minimum principal strain on the *xy* plane can be expressed as:

$$\begin{aligned} \varepsilon_{p_1}^{xy} &= \frac{\varepsilon_x + \varepsilon_y}{2} + \sqrt{\left(\frac{\varepsilon_x - \varepsilon_y}{2}\right)^2 + \left(\frac{\gamma_{xy}}{2}\right)^2} \\ \varepsilon_{p_2}^{xy} &= \frac{\varepsilon_x + \varepsilon_y}{2} - \sqrt{\left(\frac{\varepsilon_x - \varepsilon_y}{2}\right)^2 + \left(\frac{\gamma_{xy}}{2}\right)^2} \end{aligned} \tag{5}$$

$$\theta_{p_2}^{xy} = \begin{cases} \frac{1}{2}\tan^{-1}\left(\frac{\gamma_{xy}}{\varepsilon_x - \varepsilon_y}\right), & \text{if } \varepsilon_x \le \varepsilon_y \\ \frac{1}{2}\tan^{-1}\left(\frac{\gamma_{xy}}{\varepsilon_x - \varepsilon_y}\right) + \frac{\pi}{2}, & \text{if } \varepsilon_x > \varepsilon_y \end{cases} \tag{6}$$

where $\varepsilon_{p_1}^{xy}$ and $\varepsilon_{p_2}^{xy}$ are the maximum and minimum principal strains on the *xy* plane, respectively, and $\theta_{p_2}^{xy}$ is the principal angle of $\varepsilon_{p_2}^{xy}$ measured from the positive *x* axis. Substituting Eq. (4) into (5) and (6) yields:

$$\begin{aligned} \varepsilon_{p_1}^{xy} &= \cos^2 A_2 \cdot \varepsilon_{x'x'} + \sin^2 A_2 \cdot \varepsilon_{z'z'} = \left(\cos^2 A_2 \cdot \alpha_a + \sin^2 A_2 \cdot \alpha_c\right)\Delta T \\ \varepsilon_{p_2}^{xy} &= \varepsilon_{x'x'} = \alpha_a \cdot \Delta T \\ \theta_{p_2}^{xy} &= A_1 \end{aligned} \tag{7}$$

Similarly, the principal strains and principal angle on the adjacent *yz* plane (perpendicular to the *xy* plane) can be expressed as:

$$\begin{aligned} \varepsilon_{p_1}^{yz} &= \frac{\varepsilon_y + \varepsilon_z}{2} + \sqrt{\left(\frac{\varepsilon_y - \varepsilon_z}{2}\right)^2 + \left(\frac{\gamma_{yz}}{2}\right)^2} \\ \varepsilon_{p_2}^{yz} &= \frac{\varepsilon_y + \varepsilon_z}{2} - \sqrt{\left(\frac{\varepsilon_y - \varepsilon_z}{2}\right)^2 + \left(\frac{\gamma_{yz}}{2}\right)^2} \end{aligned} \tag{8}$$

$$\theta_{p_2}^{yz} = \begin{cases} \frac{1}{2}\tan^{-1}\left(\frac{\gamma_{yz}}{\varepsilon_y - \varepsilon_z}\right), & \text{if } \varepsilon_y \le \varepsilon_z \\ \frac{1}{2}\tan^{-1}\left(\frac{\gamma_{yz}}{\varepsilon_y - \varepsilon_z}\right) + \frac{\pi}{2}, & \text{if } \varepsilon_y > \varepsilon_z \end{cases} \tag{9}$$

where $\varepsilon_{p_1}^{yz}$ and $\varepsilon_{p_2}^{yz}$ are the maximum and minimum principal strains on the *yz* plane, respectively, and $\theta_{p_2}^{yz}$ is the principal angle of $\varepsilon_{p_2}^{yz}$ measured from the positive *y* axis. Substituting Eq. (4) into (8) and (9) yields:

$$\begin{aligned} \varepsilon_{p_1}^{yz} &= \sin^2 A_2 \cdot \sin^2 A_1 \cdot \varepsilon_{x'x'} + \left(\cos^2 A_2 + \sin^2 A_2 \cos^2 A_1\right) \cdot \varepsilon_{z'z'} \\ &= \left[\sin^2 A_2 \cdot \sin^2 A_1 \cdot \alpha_a + \left(\cos^2 A_2 + \sin^2 A_2 \cos^2 A_1\right) \cdot \alpha_c\right]\Delta T \\ \varepsilon_{p_2}^{yz} &= \varepsilon_{x'x'} = \alpha_a \cdot \Delta T \\ \theta_{p_2}^{yz} &= \tan^{-1}\left(\frac{\sin A_2 \cdot \cos A_1}{\cos A_2}\right) \end{aligned} \tag{10}$$

It is important to note that the magnitude of the minimum principal strain remains constant regardless of the plane, because the CTE on the *x'y'* plane is isotropic. More details about the constant minimum principal strain on surfaces will be discussed later.

From Eqs. (7) and (10), α_a and α_c can be expressed as:

$$\begin{aligned} \alpha_a &= \frac{\varepsilon_{p_2}^{xy}}{\Delta T} \\ \alpha_c &= \frac{\varepsilon_{p_1}^{xy}}{\sin^2 A_2 \Delta T} - \cot^2 A_2 \cdot \alpha_a \end{aligned} \tag{11}$$

where $A_2 = \tan^{-1}\left(\frac{\tan\theta_{p_2}^{yz}}{\cos\theta_{p_2}^{xy}}\right)$.

Similar derivations can be made using $\varepsilon_{p_1}^{yz}$ and $\varepsilon_{p_2}^{yz}$.

$$\begin{aligned} \alpha_a &= \frac{\varepsilon_{p_2}^{yz}}{\Delta T} \\ \alpha_c &= \frac{\frac{\varepsilon_{p_1}^{yz}}{\Delta T} - \sin^2 A_2 \cdot \sin^2 A_1 \cdot \alpha_a}{\cos^2 A_2 + \sin^2 A_2 \cos^2 A_1} = \frac{\frac{\varepsilon_{p_1}^{yz}}{\Delta T} - \sin^2 A_2 \cdot \sin^2 \theta_{p_2}^{xy} \cdot \alpha_a}{\cos^2 A_2 + \sin^2 A_2 \cos^2 \theta_{p_2}^{xy}} \end{aligned} \tag{12}$$

The CTE values can be determined by either (11) or (12) if the engineering strains on two perpendicular surfaces are available. It is worth noting that the value of α_a can be calculated using the strains of a single surface.

3. CTE measurements

A full-field optical technique called moiré interferometry is used to measure the surface strains. The method is described briefly first and results obtained from two specimens are presented.

3.1. Experimental method: moiré interferometry

Moiré interferometry is a full-field optical technique to measure in-plane deformations with high sensitivity, high signal-to-noise ratio, and excellent clarity. The outputs are the contour maps of in-plane displacements.

In this method, a cross-line high frequency diffraction grating, f_s, of 1200 lines per mm is replicated on a specimen surface, and it deforms together with the underlying specimen. As illustrated in Fig. 4a, a virtual reference grating, f, is formed by two coherent beams of light. The deformed specimen grating and the uniform reference grating interact to produce moiré patterns of in-plane displacements. It has been used widely for electronic packaging design and reliability assessment [14–28]. A detailed description of moiré interferometry can be found in Ref. [14].

The resultant fringe patterns represent contours of two in-plane x and y displacements, u_x and u_y, which are related to the fringe orders by [14]:

$$u_x(x,y) = \frac{1}{f}N_x(x,y), \qquad u_y(x,y) = \frac{1}{f}N_y(x,y) \tag{13}$$

where N is the fringe order and f is the frequency of the virtual reference grating. In routine practice, a virtual reference grating with a frequency of 2400 lines/mm is used, which provides a contour interval of 417 nm per fringe order. The engineering in-plane strains can be determined from the displacements by:

$$\varepsilon_x(x,y) = \frac{\partial u_x}{\partial x} = \frac{1}{f}\frac{\partial N_x(x,y)}{\partial x} \tag{14}$$

$$\varepsilon_y(x,y) = \frac{\partial u_y}{\partial y} = \frac{1}{f}\frac{\partial N_y(x,y)}{\partial y} \tag{15}$$

$$\gamma_{xy}(x,y) = \frac{\partial u_x}{\partial y} + \frac{\partial u_y}{\partial x} = \frac{1}{f}\left(\frac{\partial N_x(x,y)}{\partial y} + \frac{\partial N_y(x,y)}{\partial x}\right) \tag{16}$$

In this work, an advanced moiré interferometry system was used to document the required deformation fields. The system is illustrated schematically in Fig. 4b [28]. It consists of (1) a portable engineering moiré interferometer (PEMI) that provides two sets of virtual reference gratings, (2) a conduction chamber built on a high performance thermo-electric cooler that provides accurate temperature control, and (3) a high-resolution digital camera with a microscope objective lens. The thermal conduction chamber is mounted on an x-y-z translation stage, which allows positioning as well as focusing the specimen. More details of the system can be found in Ref. [28].

3.2. Specimen preparation: specimen with a single grain

An aluminum mold with cube shape holes was used to control the shape of solder specimen ($\approx$1 mm $\times$ 1 mm $\times$ 1 mm). A detailed procedure to fabricate the solder specimens is shown schematically

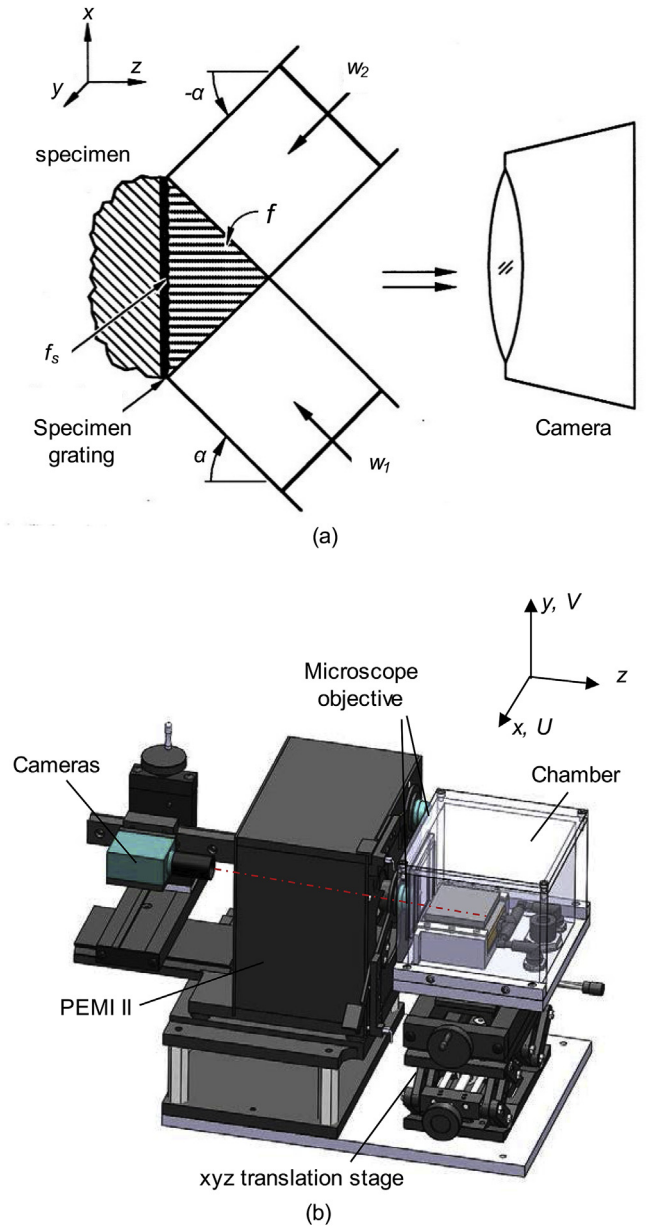

Fig. 4. Schematic illustration of (a) the principle of moiré interferometry and (b) the optical/mechanical configuration of an advanced portable moiré system.

in Fig. 5. The mold was first mounted on an aluminum substrate. They were placed on a plate heater, which was heated to 240 °C. When the mold temperature reached the steady state (about 235 °C), SAC305 solder wire was manually fed into the holes in the mold. After placing a thin hot aluminum plate on the top of the

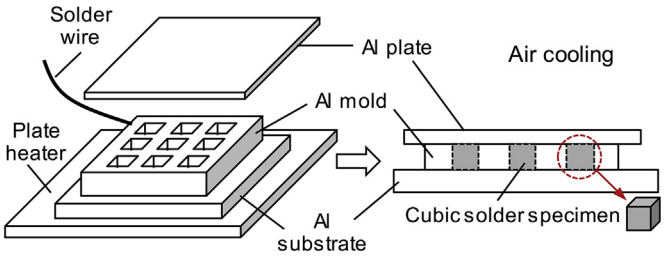

Fig. 5. Solder specimen fabrication procedure.

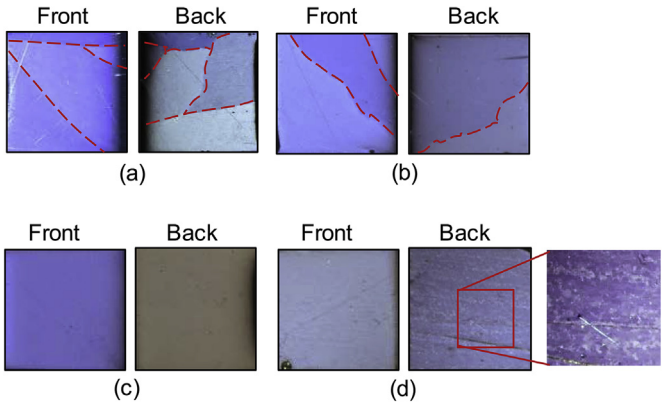

Fig. 6. Polarizing microscope images of SAC305 solder specimens fabricated at different cooling rates: (a) 25 °C/sec, (b) 3.5 °C/sec, (c) 0.8 °C/sec and (d) 0.1 °C/min.

mold, the whole assembly was removed from the heater and was cooled by natural convection. When temperature decreased to around 190 °C, the solder was completely solidified, and the assembly was moved to a metal heat sink for faster cooling. There was virtually no wetting between SAC305 solder and the aluminum mold, and thus the solder specimens were readily removed from the mold.

Several SAC305 solder grains can be produced during the solidification process. The cooling rate during the solidification process is known to be one of the most critical parameters that influence grain growth [29]. By controlling the substrate thickness and ambient conditions during the cooling process, different cooling rates were achieved.

All specimens were ground and polished after separation from the mold. The number of grains on specimen surfaces was examined using a polarizing microscope. The results of specimens fabricated at different cooling rates are shown in Fig. 6: (a) 25 °C/sec by water cooling; (b) 3.5 °C/sec by natural convection; (c) 0.8 °C/sec by natural convection cooling but with a thicker Al substrate; (d) 0.1 °C/min by a combination of conduction cooling and forced convection cooling with proportional-integral-derivative (PID) control. As expected, several grains were observed on surfaces when a cooling rate was highest (case a) while many interlaced grain structures were observed when the extremely slow cooling rate was used (case d).

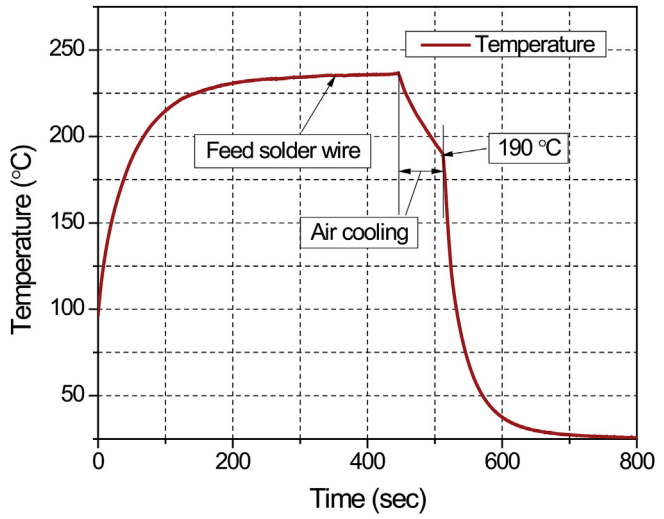

Fig. 7. Solder reflow profile for the single grain specimens.

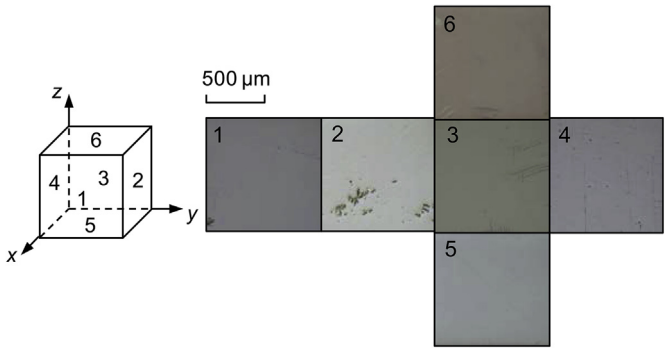

Fig. 8. Polarizing microscope images obtained from all 6 surfaces of a single-grain specimen.

The solder specimens with a single grain were obtained with a cooling rate of approximately 0.8 °C/sec. The temperature profile of the mold used in this study is shown in Fig. 7. The polarizing microscope images obtained from all 6 surfaces of a single-grain specimen are shown in Fig. 8. The results confirm that the specimen contain a single grain.

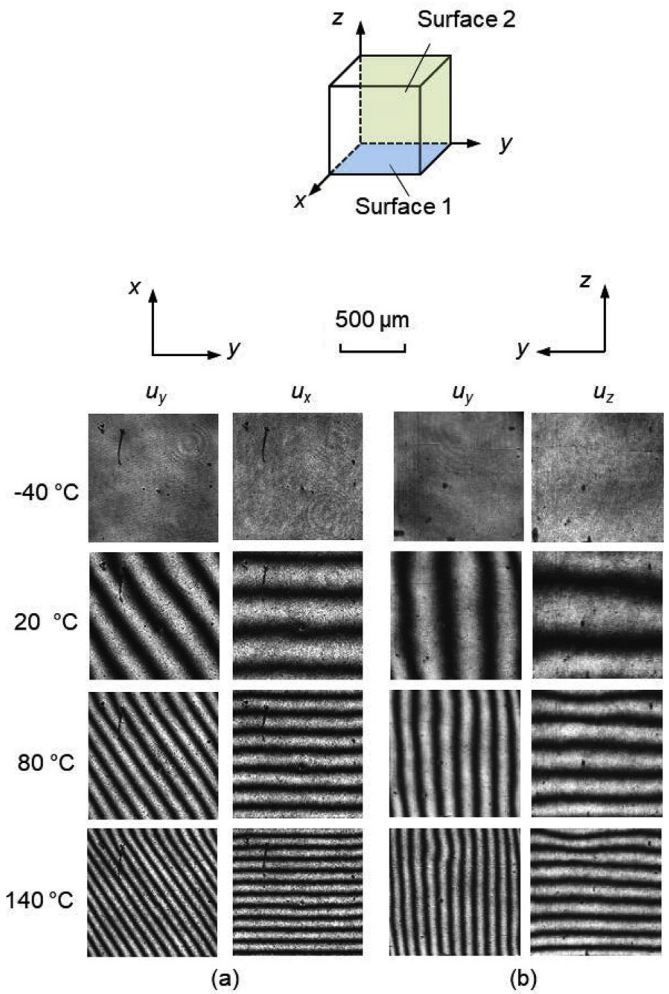

Fig. 9. Moiré fringe patterns obtained from two surfaces of Specimen 1, where the contour interval is 417 nm/fringe: (a) on the *xy* plane; (b) on the *yz* plane.

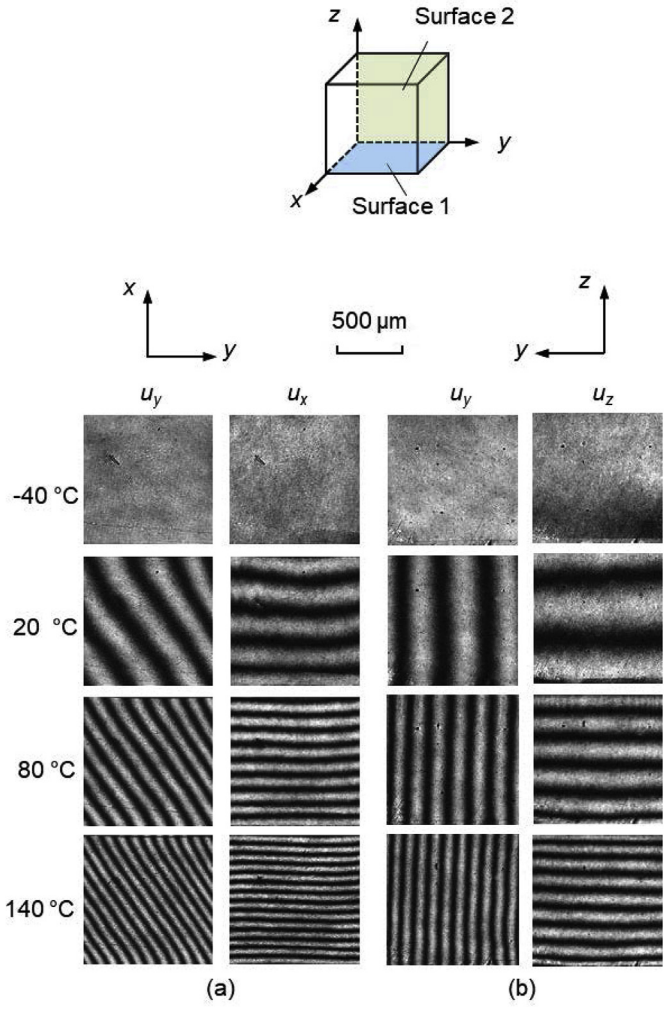

Fig. 10. Moiré fringe patterns obtained from two surfaces of Specimen 2, where the contour interval is 417 nm/fringe: (a) on the *xy* plane; (b) on the *yz* plane.

Two single-grain specimens were prepared for CTE measurements (will be referred to as Specimen 1 and Specimen 2). The specimen gratings ($f_s = 1200$ lines/mm) were replicated on two surfaces of each specimen at room temperature. The details about grating replication procedures can be found in Refs. [14,17].

3.3. Displacement fields and CTE values

A total of four moiré experiments were conducted (two surfaces of each specimen). The in-plane displacement fields (u_x, u_y on the *xy* plane and u_y, u_z on the *yz* plane) were documented at −40, 20, 80, and 140 °C. The fringe patterns of Specimens 1 and 2, representing the displacement fields, are shown in Fig. 9 and Fig. 10, respectively. In each figure, the displacements of the *xy* plane are shown in (a), and the displacements of the *yz* plane in (b).

The moiré interferometer was tuned to produce null fields (i.e., fields devoid of fringes) at −40 °C; the optical configuration was adjusted until the frequency of the virtual reference gratings were exactly twice as high as that of the specimen gratings at −40 °C.

The engineering normal and shear strains (ε_x, ε_y, ε_z, γ_{xy}, γ_{yz}) were calculated from the fringe patterns using Eqs. (14)–(16). The results are summarized in Table 1 and Table 2 for Specimens 1 and 2, respectively. Two Euler angles (A_1, A_2) were calculated from the engineering strains using Eqs. (7) and (10). The values are shown in Table 3. The averaged values (Specimen 1: $A_1 = 132.2°$ and $A_2 = -88.4°$; Specimen 2: $A_1 = 122.8°$ and $A_2 = 87.3°$) were used to conduct the subsequent CTE calculations.

The CTE values (α_a, α_c) over each temperature range were calculated using Eqs. (11) and (12). The results are summarized in Table 4 and Table 5. It is important to recall that the values of α_a can be calculated using the strains of a single surface. The variations of the α_a value from all four surfaces are less than 1 ppm/°C, which establishes the accuracy of the measurements.

The averaged CTE values of two specimens are plotted as a function of temperature in Fig. 11. As expected, the CTE value along the *c*-axis ([001] direction) is much larger than the value along the *a*-axis ([100] direction). There is clearly linear dependency of the CTE values on the temperature. The temperature dependent CTE values over a temperature range of −40 °C to 140 °C can be expressed as:

Table 3
Euler angles.

Temperature range (°C)	Mean temperature (°C)	Euler angle (degree)			
		Specimen 1		Specimen 2	
		A_1	A_2	A_1	A_2
−40 to 20	−10	132.9	−88.6	122.2	86.8
20 to 80	50	132.4	−88.4	122.5	88.1
80 to 140	110	131.2	−88.3	123.9	87.1
Average		132.2	−88.4	122.8	87.3

Table 1
Engineering strains obtained from fringe patterns of Specimen 1.

Temperature range (°C)	Mean temperature (°C)	Surface 1			Surface 2		
		ε_x (10^{-3})	ε_y (10^{-3})	γ_{xy} (10^{-3})	ε_y (10^{-3})	ε_z (10^{-3})	γ_{yz} (10^{-3})
−40 to 20	−10	1.55	1.48	0.96	1.48	1.05	−0.03
20 to 80	50	1.63	1.54	0.99	1.55	1.10	−0.04
80 to 140	110	1.73	1.60	1.04	1.62	1.13	−0.04

Table 2
Engineering strains obtained from fringe patterns of Specimen 2.

Temperature range (°C)	Mean temperature (°C)	Surface 1			Surface 2		
		ε_x (10^{-3})	ε_y (10^{-3})	γ_{xy} (10^{-3})	ε_y (10^{-3})	ε_z (10^{-3})	γ_{yz} (10^{-3})
−40 to 20	−10	1.66	1.26	0.83	1.30	1.03	0.06
20 to 80	50	1.73	1.33	0.86	1.39	1.10	0.04
80 to 140	110	1.83	1.47	0.88	1.44	1.12	0.06

Table 4
CTE values obtained from Specimen 1.

Temperature range (°C)	Mean temperature (°C)	Specimen 1			
		Based on Eq. (11)		Based on Eq. (12)	
		α_a (ppm/°C)	α_c (ppm/°C)	α_a (ppm/°C)	α_c (ppm/°C)
−40 to 20	−10	17.2	33.2	17.5	33.6
20 to 80	50	18.1	34.8	18.3	35.4
80 to 140	110	19.0	36.5	18.8	36.8

Table 5
CTE values obtained from Specimen 2.

Temperature range (°C)	Mean temperature (°C)	Specimen 2			
		Based on Eq. (11)		Based on Eq. (12)	
		α_a (ppm/°C)	α_c (ppm/°C)	α_a (ppm/°C)	α_c (ppm/°C)
−40 to 20	−10	16.6	32.0	17.2	32.7
20 to 80	50	17.6	33.5	18.3	34.8
80 to 140	110	19.6	35.5	18.6	36.9

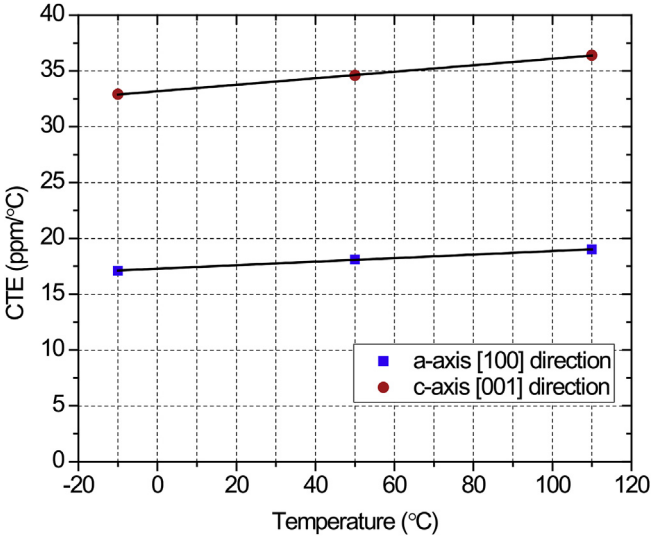

Fig. 11. Anisotropic CTE values as a function of temperature.

$$\begin{cases} \alpha_a(\text{ppm}/^\circ\text{C}) = 17.28 + 0.016T(^\circ\text{C}) \\ \alpha_c(\text{ppm}/^\circ\text{C}) = 33.18 + 0.029T(^\circ\text{C}) \end{cases} \quad (17)$$

4. Discussion: grain orientation

Determination of the grain orientation is critical to accurate calculation of the CTE values. As illustrated in Fig. 12, lines *OE* and *OF* define the angles of the minimum principal strains, $\theta_{p_2}^{xy}$ and $\theta_{p_2}^{yz}$, respectively. The vectors representing the lines can be expressed as:

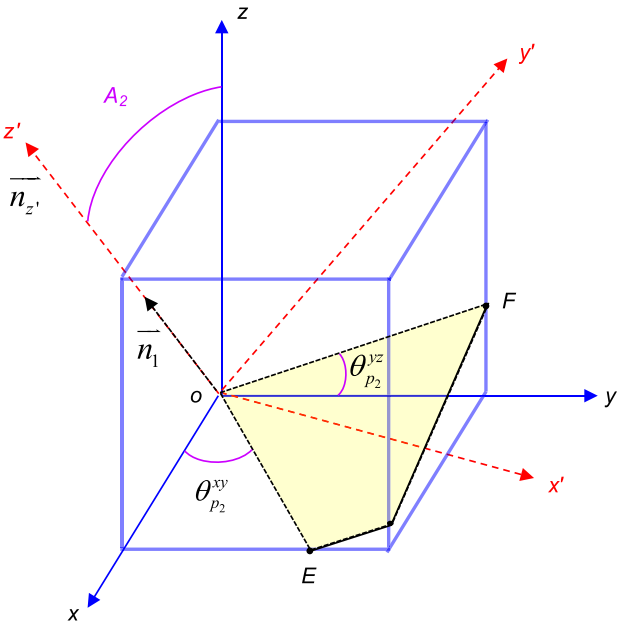

Fig. 12. Principle angles and grain orientation.

$$\begin{cases} \overrightarrow{OE} = \left[\cos\theta_{p_2}^{xy},\ \sin\theta_{p_2}^{xy},\ 0\right] \\ \overrightarrow{OF} = \left[0,\ \cos\theta_{p_2}^{yz},\ \sin\theta_{p_2}^{yz}\right] \end{cases} \quad (18)$$

Substituting Eqs. (7) and (10) into (18) yields:

$$\begin{cases} \overrightarrow{OE} = [\cos A_1,\ \sin A_1,\ 0] \\ \overrightarrow{OF} = [0,\ \cos A_2,\ \sin A_2 \cos A_1] \end{cases} \quad (19)$$

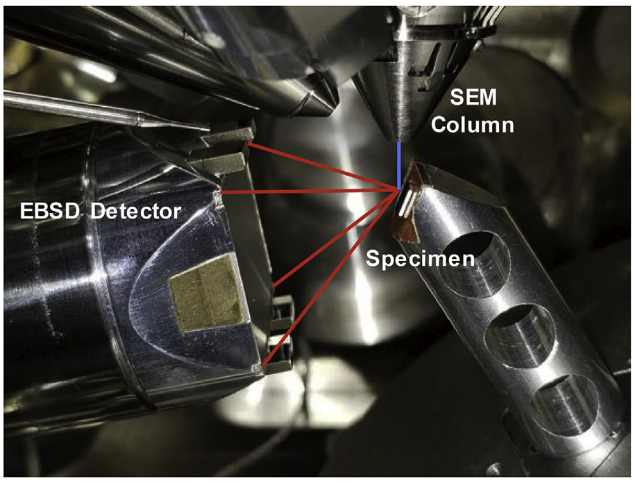

Fig. 13. Schematic of EBSD measurement system.

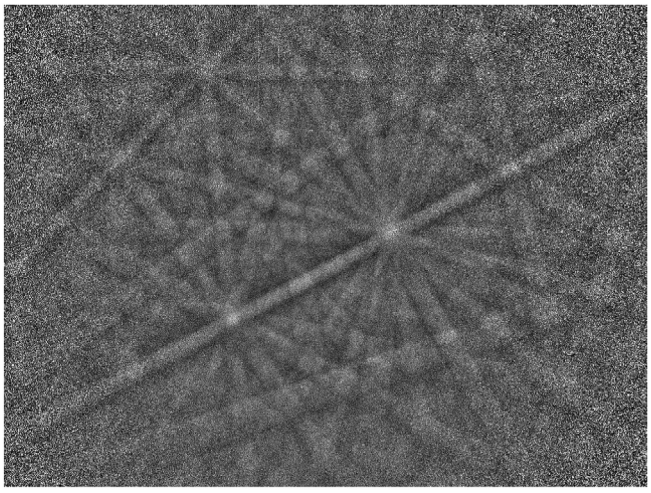

(a)

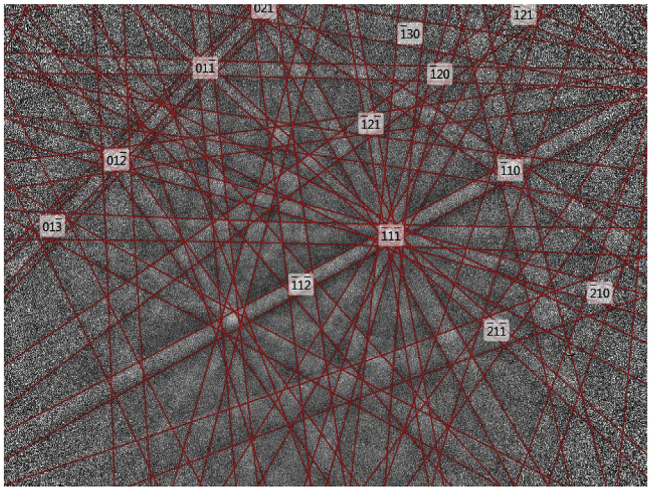

(b)

Fig. 14. EBSP captured on Surface 1 of Specimen 1: (a) original, and (b) indexed.

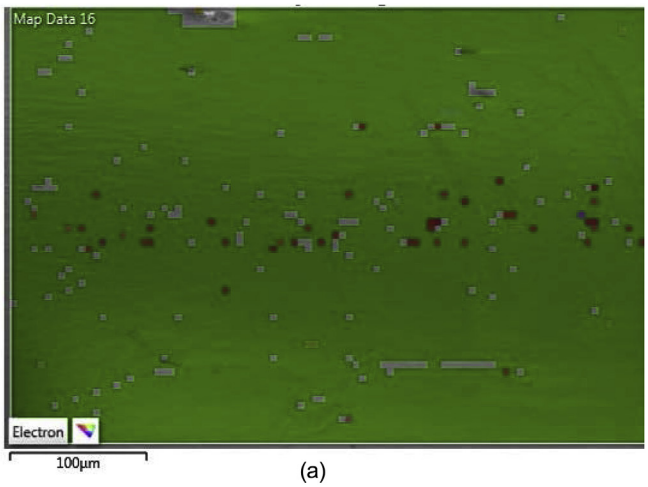

(a)

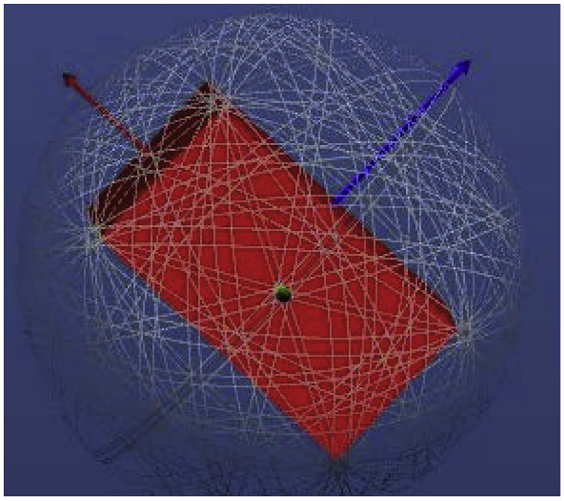

Euler angles: (136.7°; 87.8°; 5.3°)

(b)

Fig. 15. EBSD result on Surface 1 of Specimen 1: (a) EBSD layered image, and (b) grain orientation.

Then, the unit vector $\vec{n_1}$ perpendicular to the plane defined by $\vec{OE}$ and $\vec{OF}$ can be expressed as:

$$\vec{n_1} = \frac{\vec{OE} \times \vec{OF}}{\left|\vec{OE}\right| \cdot \left|\vec{OF}\right|} = [\sin A_1 \sin A_2, -\cos A_1 \sin A_2, \cos A_2] \tag{20}$$

The above unit vector, $\vec{n_1}$, in the specimen coordinate (o-xyz), can be expressed in the grain coordinate (o-$x'y'z'$) using the coordinate transformation as:

$$\vec{n_1} = \tilde{T}[\sin A_1 \sin A_2, -\cos A_1 \sin A_2, \cos A_2]^T = [0, 0, 1] = \vec{n_{z'}} \tag{21}$$

The above result indicates that $\vec{n_1}$ and $\vec{n_{z'}}$ are the same vector confirming that the plane defined by $\vec{OE}$ and $\vec{OF}$ coincides with the $x'y'$ plane in the grain coordinate.

This was further confirmed by a supplementary experiment using electron backscatter diffraction (EBSD) technique. The technique has been used widely to characterize the microstructural crystallography of any crystalline or polycrystalline materials [30].

Specimen 1 was placed in the SEM chamber, and an EBSD measurement was made on Surface 1. The incident electron beam interacted with the surface of the specimen and formed a characteristic pattern known as Kikuchi bands on the phosphor screen of the EBSD detector, as shown in Fig. 13. The electron backscatter pattern (EBSP) (Fig. 14a) was captured by a CCD and saved in a computer, which performed a Hough transform and comparison to database values for the material. The software indexed the pattern with the crystallographic data (Fig. 14b) to confirm the material phase and orientation.

The result is shown in Fig. 15. Fig. 15 (a) shows an EBSD layered image, where the uniform color indicates that the specimen contains only one grain. Based on the Euler angles obtained from the EBSD measurement, the direction vector of the *c*-axis in the specimen coordinate (Fig. 9) was determined. It is [-0.738, −0.675, 0.032], which is very close to the values calculated from the moiré results using Eq. (20) [-0.727, −0.685, 0.038].

5. Conclusion

The anisotropic CTE values of SAC305 solder were measured. Theoretical relationships among (1) the transversely-isotropic CTEs, (2) the surface strains of a specimen containing a single grain with arbitrary orientation, and (3) the grain orientation were derived first. Two cube shape specimens that contained a single grain of SAC305 were fabricated by controlling cooling rates. The surface strains were calculated on two perpendicular surfaces of each specimen as a function of temperature from displacement fields obtained by moiré interferometry. Two directional CTE values were determined from the strains by the theoretical relationships. The *c*-axis direction determined from the test was compared with the grain orientation obtained by the electron backscatter diffraction (EBSD) method. The comparison corroborated the validity of the CTE measurements.

References

[1] G. Cuddalorepatta, Evolution of the Microstructure and Viscoplastic Behavior of Microscale SAC305 Solder Joints as a Function of Mechanical Fatigue Damage, dissertation, University of Maryland, College Park, 2010.

[2] C. Basaran, J. Jiang, Measuring intrinsic elastic modulus of Pb/Sn solder alloys, Mech. Mater. 34 (6) (2002) 349–362.

[3] H. Tang, C. Basaran, Influence of microstructure coarsening on thermo-mechanical fatigue behavior of Pb/Sn eutectic solder joints, Int. J. Damage Mech. 10 (3) (2001) 235–255.

[4] S. Mukherjee, B. Zhou, A. Dasgupta, T.R. Bieler, Multiscale modeling of the anisotropic transient creep response of heterogeneous single crystal SnAgCu solder, Int. J. Plast. 78 (2016) 1–25.

[5] D.W. Henderson, J.J. Woods, T.A. Gosselin, J. Bartelo, D.E. King, T. Korhonen, M. Korhonen, L. Lehman, E. Cotts, S.K. Kang, The microstructure of Sn in near-eutectic Sn–Ag–Cu alloy solder joints and its role in thermomechanical fatigue, J. Mater. Res. 19 (6) (2004) 1608–1612.

[6] T.R. Bieler, H. Jiang, L.P. Lehman, T. Kirkpatrick, E.J. Cotts, B. Nandagopal, Influence of Sn grain size and orientation on the thermomechanical response and reliability of Pb-free solder joints, IEEE Trans. Compon. Packag. Technol. 31 (2) (2008) 370–381.

[7] T.-K. Lee, B. Zhou, L. Blair, K.-C. Liu, T.R. Bieler, Sn-Ag-Cu solder joint microstructure and orientation evolution as a function of position and thermal cycles in ball grid arrays using orientation imaging microscopy, J. Electron. Mater. 39 (12) (2010) 2588–2597.

[8] D.A. Shnawah, M.F.M. Sabri, I.A. Badruddin, A review on thermal cycling and drop impact reliability of SAC solder joint in portable electronic products, Microelectron. Reliab. 52 (1) (2012) 90–99.

[9] S. Park, R. Dhakal, L. Lehman, E.J. Cotts, Grain deformation and strain in board level SnAgCu solder interconnects under deep thermal cycling, IEEE Trans. Compon. Packag. Technol. 30 (1) (2007) 178–185.

[10] H. Chen, B. Yan, M. Yang, X. Ma, M. Li, Effect of grain orientation on mechanical properties and thermomechanical response of Sn-based solder interconnects, Mater. Char. 85 (2013) 64–72.

[11] V. Deshpande, D. Sirdeshmukh, Thermal expansion of tetragonal tin, Acta Crystallogr. 14 (4) (1961) 355–356.

[12] V. Deshpande, D. Sirdeshmukh, Thermal expansion of tin in the β–γ transition region, Acta Crystallogr. 15 (3) (1962) 294–295.

[13] J.J. Sundelin, S.T. Nurmi, T.K. Lepistö, Recrystallization behaviour of SnAgCu solder joints, Materials Science and Engineering: a 474 (1) (2008) 201–207.

[14] D. Post, B. Han, P. Ifju, High Sensitivity Moiré: Experimental Analysis for Mechanics and Materials, Mechanical Engineering Series, Springer-Verlag, NY, 1994. Student edition, 1997.

[15] Y. Guo, C.K. Lim, W.T. Chen, C.G. Woychik, Solder ball connect (SBC) assemblies under thermal loading: I. Deformation measurement via moiré interferometry, and its interpretation, IBM J. Res. Dev. 37 (5) (1993) 635–648.

[16] B. Han, Y. Guo, Determination of an effective coefficient of thermal expansion of electronic packaging components: a whole-field approach, IEEE Trans. Compon. Packag. Manuf. Technol. 19 (2) (1996) 240–247.

[17] B. Han, Recent advancements of moiré and microscopic moiré interferometry for thermal deformation analyses of microelectronics devices, Exp. Mech. 38 (4) (1998) 278–288.

[18] J.-H. Zhao, X. Dai, P.S. Ho, Analysis and modeling verification for thermal-mechanical deformation in flip-chip packages, in: Proceedings of the 48th IEEE International Conference on Electronic Components and Technology Conference (ECTC), IEEE, 1998, pp. 336–344.

[19] B. Han, P. Kunthong, Micro-mechanical deformation analysis of surface laminar circuit in organic flip-chip package: an experimental study, Transactions-american Society of Mechanical Engineers Journal of Electronic Packaging 122 (4) (2000) 294–300.

[20] S. Cho, B. Han, Observing real-time thermal deformations in electronic packaging, Exp. Tech. 26 (3) (2002) 25–29.

[21] S.-J. Ham, W.-S. Kwon, K.-W. Paik, S.-B. Lee, In-situ moire measurement of adhesive flip-chip bonded assembly under thermal cycling condition, in: Proceedings of the 2nd IEEE International Conference on Polymers and Adhesives in Microelectronics and Photonics, IEEE, 2002, pp. 63–67.

[22] B. Han, Thermal stresses in microelectronics subassemblies: quantitative characterization using photomechanics methods, J. Therm. Stresses 26 (6) (2003) 583–613.

[23] S. Cho, B. Han, J. Joo, Temperature dependent deformation analysis of ceramic ball grid array package assembly under accelerated thermal cycling condition, Transactions-American Society of Mechanical Engineers Journal of Electronic Packaging 126 (1) (2004) 41–47.

[24] J. Joo, S. Cho, B. Han, Characterization of flexural and thermo-mechanical behavior of plastic ball grid package assembly using moiré interferometry, Microelectron. Reliab. 45 (3) (2005) 637–646.

[25] D.-S. Kim, B. Han, A. Yadur, P.J. Gromala, Electronic control package model calibration using moiré interferometry, in: Proceedings of the 15th IEEE International Conference on Thermal, Mechanical and Multi-physics Simulation and Experiments in Microelectronics and Microsystems (EuroSimE), IEEE, 2014, pp. 1–5.

[26] B. Wu, D.-S. Kim, B. Han, A. Palczynska, P.J. Gromala, Thermal deformation analysis of automotive electronic control units subjected to passive and active thermal conditions, in: Proceedings of the 16th IEEE International Conference on Thermal, Mechanical and Multi-physics Simulation and Experiments in Microelectronics and Microsystems (EuroSimE), IEEE, 2015, pp. 1–6.

[27] B. Wu, D.-S. Kim, B. Han, A. Palczynska, A. Prisacaru, P.J. Gromala, Hybrid approach to conduct failure prognostics of automotive electronic control unit, in: Proceedings of the 67th IEEE International Conference on Electronic Components and Technology Conference (ECTC), IEEE, 2017, pp. 476–482.

[28] B. Wu, B. Han, Advanced mechanical/optical configuration of real-time moiré interferometry for thermal deformation analysis of fan-out wafer level package, IEEE Trans. Compon. Packag. Manuf. Technol. 8 (5) (2018) 764–772.

[29] M. Mueller, S. Wiese, M. Roellig, K.-J. Wolter, Effect of composition and cooling rate on the microstructure of SnAgCu-solder joints, in: Proceedings of the 57th IEEE International Conference on Electronic Components and Technology Conference (ECTC), IEEE, 2007, pp. 1579–1588.

[30] O. Engler, V. Randle, Introduction to Texture Analysis: Macrotexture, Microtexture, and Orientation Mapping, CRC press, 2009.